

Article

Effects of Central Metal Ion on Binuclear Metal Phthalocyanine-Based Redox Mediator for Lithium Carbonate Decomposition

Qinghui Yan ^{1,4,†}, Linghui Yan ^{3,†}, Haoshen Huang ², Zhengfei Chen ², Zixuan Liu ^{2,4,*}, Shaodong Zhou ^{3,*}  and Haiyong He ⁴

¹ School of Materials Science and Chemical Engineering, Ningbo University, Ningbo 315211, China; 2111086218@nbu.edu.cn

² School of Biological and Chemical Engineering, NingboTech University, Ningbo 315100, China; 13685729957@163.com (H.H.); zhengfei.chen@nbt.edu.cn (Z.C.)

³ College of Chemical and Biological Engineering, Zhejiang University, Hangzhou 310058, China; lhyan@zju.edu.cn

⁴ Ningbo Institute of Materials Technology and Engineering, Chinese Academy of Sciences, Ningbo 315201, China; hehaiyong@nimte.ac.cn

* Correspondence: liuzixuan@nbt.edu.cn (Z.L.); szhou@zju.edu.cn (S.Z.); Tel.: +86-574-882-295-98 (Z.L.); +86-571-879-516-15 (S.Z.)

† These authors contributed equally to this work.

Abstract: Li_2CO_3 is the most tenacious parasitic solid-state product in lithium–air batteries (LABs). Developing suitable redox mediators (RMs) is an efficient way to address the Li_2CO_3 issue, but only a few RMs have been investigated to date, and their mechanism of action also remains elusive. Herein, we investigate the effects of the central metal ion in binuclear metal phthalocyanines on the catalysis of Li_2CO_3 decomposition, namely binuclear cobalt phthalocyanine (bi-CoPc) and binuclear cobalt manganese phthalocyanine (bi-CoMnPc). Density functional theory (DFT) calculations indicate that the key intermediate peroxydicarbonate ($^*\text{C}_2\text{O}_6^{2-}$) is stabilized by bi-CoPc²⁺ and bi-CoMnPc³⁺, which is accountable for their excellent catalytic effects. With one central metal ion substituted by manganese for cobalt, the bi-CoMnPc's second active redox couple shifts from the second Co(II)/Co(III) couple in the central metal ion to the Pc(-2)/Pc(-1) couple in the phthalocyanine ring. In artificial dry air ($\text{N}_2\text{-O}_2$, 78:22, v/v), the LAB cell with bi-CoMnPc in electrolyte exhibited 261 cycles under a fixed capacity of 500 mAh g⁻¹_{carbon} and current density of 100 mA g⁻¹_{carbon}, significantly better than the RM-free cell (62 cycles) and the cell with bi-CoPc (193 cycles).

Keywords: lithium–air batteries; Li_2CO_3 decomposition; redox mediator; binuclear metal phthalocyanine; density functional theory



Citation: Yan, Q.; Yan, L.; Huang, H.; Chen, Z.; Liu, Z.; Zhou, S.; He, H. Effects of Central Metal Ion on Binuclear Metal Phthalocyanine-Based Redox Mediator for Lithium Carbonate Decomposition. *Molecules* **2024**, *29*, 2034. <https://doi.org/10.3390/molecules29092034>

Received: 23 February 2024

Revised: 24 April 2024

Accepted: 24 April 2024

Published: 28 April 2024



Copyright: © 2024 by the authors. Licensee MDPI, Basel, Switzerland. This article is an open access article distributed under the terms and conditions of the Creative Commons Attribution (CC BY) license (<https://creativecommons.org/licenses/by/4.0/>).

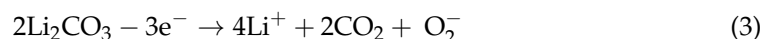
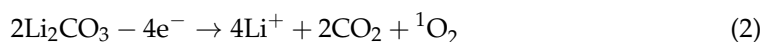
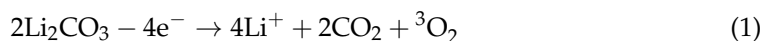
1. Introduction

Along with the fast-paced electrification, intelligentization, and mobilization of industry and daily life, the demand for energy storage devices with higher energy density becomes increasingly urgent. Lithium–air batteries (LABs) possess the highest theoretical energy density (~11,400 Wh/kg, excluding O₂ mass) among all electrochemical energy storage technologies and have drawn tremendous attention in the past two decades. However, major challenges must be conquered before the practicality of LABs, originating from the highly reactive cathode/anode materials and (intermediate) products (such as metallic lithium, ¹O₂, LiO₂, O₂⁻, etc.), as well as the unstable solid–solid contact between discharge/parasitic reaction products and the air cathode [1–4].

In LABs, Li_2CO_3 is regarded as the “Achilles’ heel” [5] because it is both virtually inevitable to form and difficult to remove. On the one hand, Li_2CO_3 can be produced both from the absorption of adventitious CO₂ and from the degradation of cell components

(electrolyte solvents, lithium salts, carbon electrodes, etc.). On the other hand, Li_2CO_3 is the most tenacious parasitic solid-state product in LABs due to its high oxidative decomposition potential, low electronic/ionic conductivity, and low solubility in most organic solvents. Containing O_2 in the battery system and converting LABs to lithium–oxygen batteries (LOBs) can mitigate Li_2CO_3 accumulation, but at the cost of greatly reduced energy density (~ 3450 Wh/kg in theory, including O_2 mass). Therefore, it is necessary to develop suitable catalysts for Li_2CO_3 decomposition to enable the utilization of ambient air, especially the redox mediators (RMs) that can overcome the solid–solid contact difficulty between solid-state Li_2CO_3 and an air cathode.

Since the first discovery of Li_2CO_3 decomposing RM (a planar binuclear cobalt phthalocyanine, bi-CoPc) [6], several other RMs have been reported effective towards Li_2CO_3 decomposition, such as LiBr [7,8], conjugated cobalt polyphthalocyanine (CoPPc) [9], cobalt tetramethoxyphenyl porphyrin (CoTMPP) [10], ruthenocene (Ruc) [11], (1*R*,2*R*)-(-)-*N,N*-bis(3,5-di-*t*-butylsalicylidene)-1,2-cyclohexanediaminocobalt(II) (salen-Co(II)) [12], *N,N,N',N'*-tetramethyl-*p*-phenylenediamine (TMPD) [13], 5,10-dimethylphenazine (DMPZ) [13], *S*-phenyl carbonothioate (SPC^-) [14], 2,5-di-*tert*-butyl-1,4-dimethoxybenzene (DBDMB) [15], etc. However, the Li_2CO_3 decomposition mechanism remains elusive. Ideally, Li_2CO_3 should decompose via Equation (1), which reverses the discharge reaction to reproduce O_2 and CO_2 ; however, numerous investigations have reported substantially less-than-stoichiometric O_2 in the evolving gas due to the undesirable decomposition paths (Equations (2) and (3)) and following $^1\text{O}_2/\text{O}_2^-$ attacks on electrolyte components [16–19]. Furthermore, the RMs' exact mechanism of action is still debated, especially the effectiveness of 1-electron RMs in catalyzing Li_2CO_3 decomposition. Our previous work proposed the necessity of 2-electron RMs [6], which is supported by some other 2- or multiple-electron ones, such as LiBr [7,8], CoPPc [9], CoTMPP [10], and SPC^- [14]. However, recently, some 1-electron RMs have also been reported to be effective, such as Ruc [11], salen-Co(II) [12], DMDMB [15], TMPD [13], DMPZ [13], etc.



In this work, a planar binuclear cobalt manganese phthalocyanine (bi-CoMnPc, structure shown in Figure S1) is comparatively tested with bi-CoPc to investigate the effects of central metal ions in binuclear metal phthalocyanines on the catalysis of Li_2CO_3 decomposition. Density functional theory (DFT) calculations indicate that the key intermediate peroxydicarbonate ($^*\text{C}_2\text{O}_6^{2-}$) is stabilized by bi-CoPc $^{2+}$ and bi-CoMnPc $^{3+}$, which is accountable for their excellent catalytic effects. With one central metal ion substituted by manganese for cobalt, the bi-CoMnPc's second active redox couple for catalyzing Li_2CO_3 decomposition shifts from the second Co(II)/Co(III) couple in the central metal ion to the Pc(−2)/Pc(−1) couple in the phthalocyanine ring. In artificial dry air, the LAB cell with bi-CoMnPc exhibited significantly improved cyclability than the RM-free one and even the cell with bi-CoPc.

2. Results and Discussion

Cyclic voltammetry (CV) in the Ar atmosphere was conducted to identify the electrochemically active redox couples in bi-CoMnPc. As displayed in Figure 1a, bi-CoMnPc shows a pair of redox peaks (marked as $1_a/1_c$) around 2.69 V vs. Li/Li $^+$, with emphasized shoulders (marked as $1'_a/1'_c$) at slightly higher potentials. These two pairs could be assigned to the Co(I)/Co(II) couple and the Pc(−3)Pc(−2)/Pc(−2)Pc(−2) couple, respectively [6,20–22]. Since their redox potentials are imposed on each other, it is difficult to exactly differentiate them. At around 3.48 V vs. Li/Li $^+$, a pair of small peaks are observed, marked as $2_a/2_c$, which are assigned to the Mn(II)/Mn(III) couple [20–22]. Adjacent to that, another pair of redox peaks (marked as $2'_a/2'_c$) appear at about 3.72 V vs. Li/Li $^+$, which is assigned to the Co(II)/Co(III) couple [6,22], similar to that in bi-CoPc ($\text{II}_a/\text{II}'_a/\text{II}_c$ in Figure 1a). At

3.9~4.2 V vs. Li/Li⁺, a pair of broad peaks (marked as 3_a/3_c) are observed in the reductive and oxidative branches, which could be assigned to the redox of phthalocyanine rings, i.e., the Pc(−2)Pc(−1)/Pc(−2)Pc(−2) and Pc(−1)Pc(−1)/Pc(−2)Pc(−1) couples [6,22], similar to that in bi-CoPc (III_a/III_c).

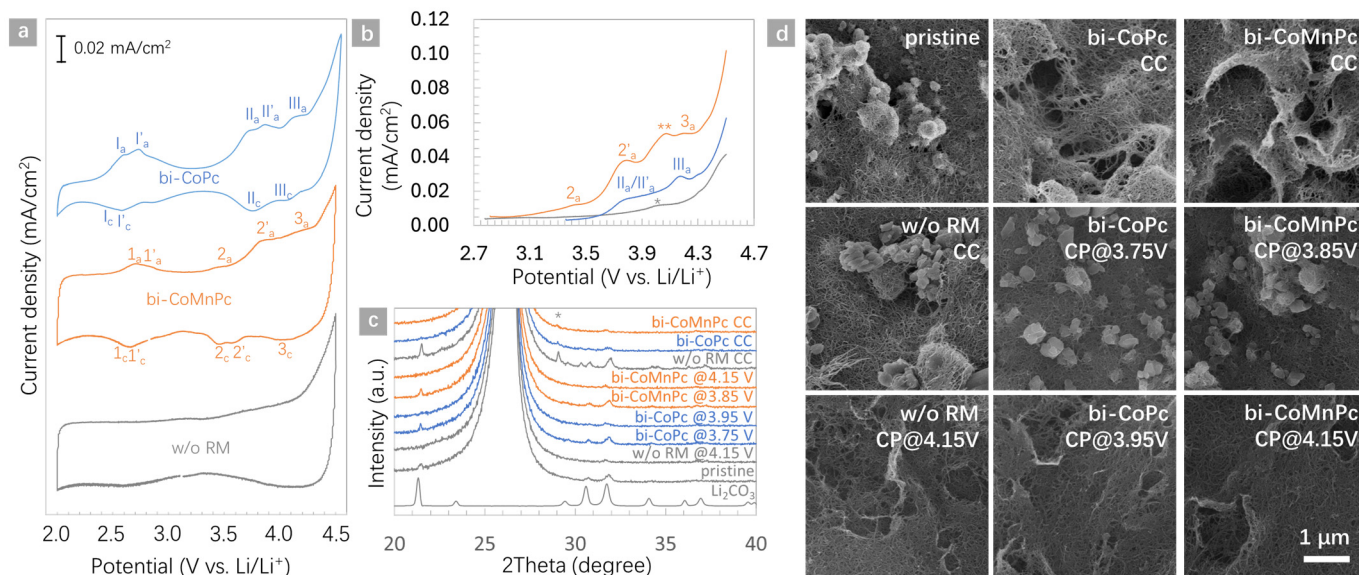


Figure 1. (a) Cyclic voltammograms of bi-CoPc and bi-CoMnPc in Ar atmosphere; (b) LSV curves of the Li₂CO₃-MWCNT composite electrodes with bi-CoMnPc, bi-CoPc, or without RM in the electrolyte, the asterisk (*) and double asterisk (**) signs mark the oxidative peaks presumably attributed to Li₂CO₃ decomposition; (c) XRD patterns of the Li₂CO₃-MWCNT composite electrodes after galvanostatic charging (marked as CC) to 4.55 V, or after potentiostatic charging at 3.75/3.95 V vs. Li/Li⁺ with bi-CoPc, at 3.85/4.15 V with bi-CoMnPc, or at 4.15 V without RM, the asterisk (*) sign marks the unknown peak; (d) SEM images of the galvanostatically or potentiostatically charged Li₂CO₃-MWCNT composite electrodes.

According to the function mechanism of RMs, the active redox couples must have higher potential than the target solid-state discharge (or parasitic) product [6–15], which is 3.71 V vs. Li/Li⁺ for Li₂CO₃ (Equation (3)); therefore, in bi-CoMnPc, the active redox couples should be the Co(II)/Co(III), Pc(−2)Pc(−1)/Pc(−2)Pc(−2) and Pc(−1)Pc(−1)/Pc(−2)Pc(−1) couples. Compared to bi-CoPc, due to the substitution of manganese for cobalt, the redox potential of the central metal ion was lowered by ~340 mV from ~3.82 V (with the Co(II)/Co(III) couple) to ~3.48 V (with the Mn(II)/Mn(III) couple). This should have two consequences: on the one hand, the lowered potential would lose the redox couple's ability to facilitate Li₂CO₃ decomposition; on the other hand, it is beneficial to facilitate the decomposition of other solid-state products such as Li₂O₂, LiOH, and carboxylates, as reported in previous works [23–25].

To investigate the feasibility of bi-CoMnPc for catalyzing Li₂CO₃ decomposition, linear scanning voltammetry (LSV), galvanostatic, and potentiostatic charging tests were conducted for Li₂CO₃-MWCNT (multiwall carbon nanotube) composite electrodes with bi-CoMnPc, bi-CoPc, or without RM in the electrolyte. As shown in Figure 1b, in the LSV test, without RM in the electrolyte, a small peak (*) emerges at 4.0 V vs. Li/Li⁺, which could be attributed to Li₂CO₃ decomposition. When bi-CoPc was added into the electrolyte, the oxidative current density was roughly doubled in the range of 3.75~4.50 V vs. Li/Li⁺, and the oxidative peaks corresponded well to II_a/II'_a and III_a as in the Li₂CO₃-free CV (Figure 1a). As for the sample with bi-CoMnPc, it is interesting to observe that the oxidative current density was further doubled than that with bi-CoPc. Furthermore, aside from the oxidative peaks 2_a, 2'_a, and 3_a (as in Figure 1a), a new peak (**) appeared at ~4.05 V vs. Li/Li⁺, which is presumably attributed to Li₂CO₃ decomposition. After galvanostatic charging, the preloaded Li₂CO₃ was almost completely removed for the samples with

bi-CoPc or bi-CoMnPc, leaving cavities in the MWCNT matrix, as characterized by X-ray diffraction (XRD) and scanning electronic microscopy (SEM) test, and shown in Figure 1c,d. In contrast, many Li_2CO_3 particles remained in the RM-free sample. Potentiostatic charging tests were also conducted, as shown in Figure 1b–d. After charging with bi-CoMnPc at 3.85 V, most of the preloaded Li_2CO_3 still remained in the carbon paper. In sharp contrast, when the charging potential increased to 4.15 V, Li_2CO_3 was almost completely removed. For comparison, the same tests were conducted with bi-CoPc at 3.75 V and 3.95 V, respectively. In accordance with our previous work [6], Li_2CO_3 remained at 3.75 V but was completely removed at 3.95 V.

Based on these results, it was demonstrated that, similar to bi-CoPc, bi-CoMnPc can also catalyze Li_2CO_3 decomposition. However, its catalysis mechanism should be a bit different from that of bi-CoPc because, unlike in bi-CoPc, the second central metal ion (Mn) in bi-CoMnPc is not redox-active for facilitating Li_2CO_3 decomposition. In our previous work, it was proposed that the RM-catalyzed Li_2CO_3 decomposition requires two electrons extracted from Li_2CO_3 to a single RM molecule rather than tandem electron transfer with different RM molecules [6]. Compared to that in bi-CoPc, the absence of the second Co(II)/Co(III) couple obliges the Pc(−2)Pc(−1)/Pc(−2)Pc(−2) couple in bi-CoMnPc to function as the second active redox couple to successfully extract electrons from Li_2CO_3 to the RM molecule and subsequently to the working electrode, thus raising the available potential for Li_2CO_3 decomposition.

To further investigate the mechanism of RM-catalyzed Li_2CO_3 decomposition, we performed DFT calculations for the Li_2CO_3 decomposition process with bi-CoPc or bi-CoMnPc. Three possible sets of reaction products, namely CO_2 and $^3\text{O}_2$, CO_2 and $^1\text{O}_2$, CO_2 and O_2^- , were considered.

The most favorable Li_2CO_3 decomposition pathways on bi-CoPc $^{2+}$ are illustrated in Figure 2a,b and Equation (4), and the other pathways and corresponding structures are shown in Figures S2–S4. With bi-CoPc $^{2+}$, upon dissociation of $\text{Li}_2\text{CO}_3(\text{s})$ from the solid phase to CO_3^{2-} and Li^+ , CO_3^{2-} adsorbs on the bi-CoPc $^{2+}$ with both the O-Co and O-C interactions. Next, another molecular CO_3^{2-} is adsorbed on the $^*\text{CO}_3^{2-}$ structure through O-O interaction to generate $^*\text{C}_2\text{O}_6^{4-}/\text{bi-CoPc}^{2+}$. And then $^*\text{C}_2\text{O}_6^{4-}$ loses two electrons to obtain $\text{C}_2\text{O}_6^{2-}$, while bi-CoPc $^{2+}$ receives two electrons to reduce back to neutral bi-CoPc. Compared to the simultaneous transfer of two electrons ($^*\text{CO}_3^{2-} \rightarrow ^*\text{C}_2\text{O}_6^{4-} \rightarrow \text{C}_2\text{O}_6^{2-}$ accompanied by $\text{bi-CoPc}^{2+} \rightarrow \text{bi-CoPc}$), the process of tandem electron transfer, as shown by the black lines in Figure 2a ($^*\text{CO}_3^{2-} \rightarrow \text{CO}_3^- \rightarrow \text{C}_2\text{O}_6^{3-} \rightarrow \text{C}_2\text{O}_6^{2-}$) is not energetically favorable, regardless of whether the two electrons are gained by $\text{bi-CoPc}^{2+} \rightarrow \text{bi-CoPc}^+ \rightarrow \text{bi-CoPc}$, $2\text{bi-CoPc}^{2+} \rightarrow 2\text{bi-CoPc}^+ \rightarrow 2\text{bi-CoPc}$ or $2\text{bi-CoPc}^+ \rightarrow 2\text{bi-CoPc}$ (see Figures S2–S4).

Subsequently, $\text{C}_2\text{O}_6^{2-}$ adsorbs on another bi-CoPc $^{2+}$ and desorbs a CO_2 molecule to produce $^*\text{CO}_4^{2-}/\text{bi-CoPc}^{2+}$. With an additional two electrons transferred from CO_4^{2-} to bi-CoPc $^{2+}$, CO_2 and $^1\text{O}_2$ are accordingly produced, as well as bi-CoPc. Though $^*\text{CO}_4^{2-}$ serves as a bifurcation point to lead to three possible sets of reaction products, namely CO_2 and $^1\text{O}_2$, CO_2 and $^3\text{O}_2$, and CO_2 and O_2^- , the production of the latter two is kinetically disadvantageous.

For the whole process of Li_2CO_3 decomposition, the crucial elementary reaction with the highest reaction energy is $^*\text{C}_2\text{O}_6^{4-}/\text{bi-CoPc}^{2+} \rightarrow \text{C}_2\text{O}_6^{2-}/\text{bi-CoPc}$ ($\Delta G_r = 328 \text{ kJ/mol}$). Considering both the thermodynamics and kinetics, the main products of Li_2CO_3 decomposition correspond to CO_2 and $^1\text{O}_2$ [6]. The preference for $^1\text{O}_2$ production over $^3\text{O}_2$ and O_2^- may help explain the unusually low O_2 evolution in Li_2CO_3 decomposition compared to that in the Li_2O_2 decomposition scenario.

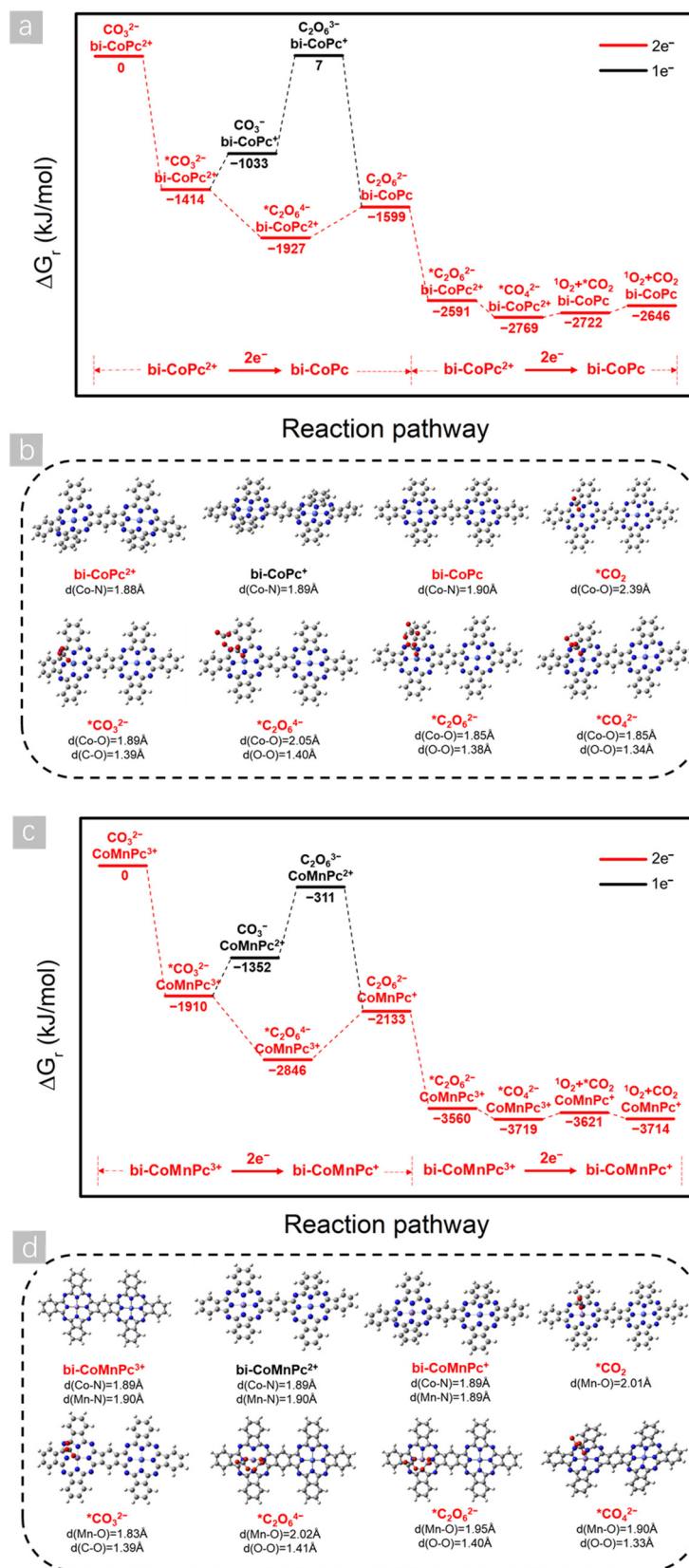
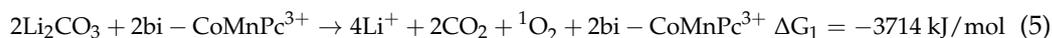
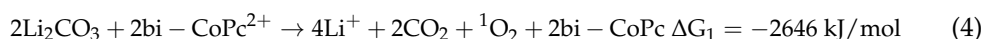
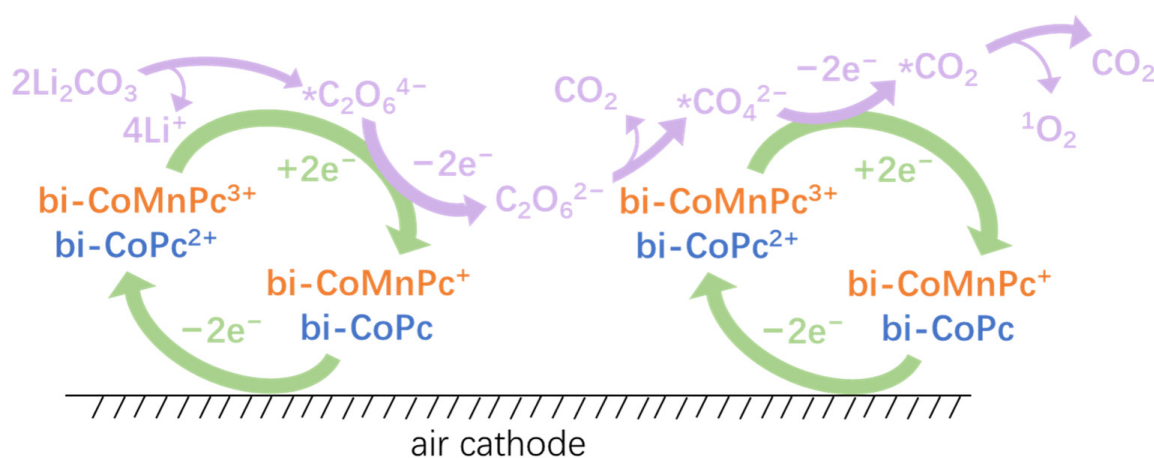


Figure 2. (a) The most favorable Li_2CO_3 decomposition pathways on bi-CoPc^{2+} ; (b) the corresponding structure evolution of Li_2CO_3 decomposition on bi-CoPc^{2+} ; (c) the most favorable Li_2CO_3 decomposition pathways on bi-CoMnPc^{3+} ; (d) the corresponding structure evolution of Li_2CO_3 decomposition on bi-CoMnPc^{3+} .



The reaction pathways for carbonate decomposition on bi-CoMnPc³⁺ are shown in Figure 2c,d and Equation (5), and more detailed information is exhibited in Figures S5–S7. Upon substitution of Mn for Co, more positive charges accumulate on Mn (the NPA charges on Mn and Co in bi-CoMnPc³⁺ are 1.262 and 0.849, respectively). Therefore, the electrostatic interaction between CO₃²⁻ and the Mn site is slightly stronger than that between CO₃²⁻ and the Co site, leading to preferable adsorption of CO₃²⁻ at the manganese site. Although the initial adsorption site of CO₃²⁻ at bi-CoMnPc³⁺ changes to Mn, the energetically most preferred reaction pathways to form soluble C₂O₆²⁻ intermediates are similar (*CO₃²⁻ → *C₂O₆⁴⁻ → C₂O₆²⁻ companies by bi-CoMnPc³⁺ → bi-CoMnPc⁺). Here, the tandem electron transfer to form C₂O₆²⁻ accompanied by bi-CoMnPc³⁺ → bi-CoMnPc²⁺ → bi-CoMnPc⁺, 2bi-CoMnPc³⁺ → 2bi-CoMnPc²⁺, or 2bi-CoMnPc²⁺ → 2bi-CoMnPc⁺ are less favorable (see Figures S5–S7). In addition, compared to the decomposition route to generate ³O₂ (Equation (1)) or O₂⁻ (Equation (3)), the reaction energy for producing ¹O₂ (Equation (2)) is also much lower, affording CO₂ and ¹O₂ as the main products with 3714 kJ/mol of energy released for the whole decomposition process, which is much higher than that in the bi-CoPc system (ΔG_r = -2646 kJ/mol). In this process, the crucial elementary reaction is *C₂O₆⁴⁻/bi-CoMnPc³⁺ → C₂O₆²⁻/bi-CoMnPc⁺. Here, the reaction energy for *C₂O₆⁴⁻ → C₂O₆²⁻ (ΔG_r = 713 kJ/mol) is much higher than that in the bi-CoPc system (ΔG_r = 328 kJ/mol). According to the experimental results, the decomposition voltage of lithium carbonate in the bi-CoMnPc system is higher than that in the bi-CoPc system.

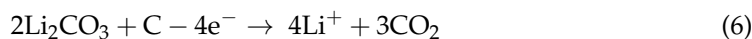
It should be noted that, in the Li₂CO₃ decomposition process, the soluble *C₂O₆²⁻ is a crucial intermediate because it can desorb and re-adsorb onto another RM molecule (or ion) or separately diffuse onto the air cathode surface to continue decomposition [8,26]. According to the calculation and discussion above, *C₂O₆²⁻ is stabilized with the facilitation of bi-CoPc⁺/bi-CoMnPc⁺/bi-CoMnPc²⁺, and even more so with bi-CoPc²⁺/bi-CoMnPc³⁺, favoring *C₂O₆²⁻ desorption and subsequent adsorption onto fresh RMs (bi-CoPc²⁺/bi-CoMnPc³⁺) or diffusion onto the air cathode to enhance the decomposition process. It can thus be deduced that, for metal phthalocyanine-type RMs, 2-electron ones are superior to 1-electron ones in facilitating Li₂CO₃ decomposition, consistent with our experimental results (Figure 1 and Ref. [6]). And the Li₂CO₃ decomposition with the bi-CoMnPc/bi-CoPc facilitation can be illustrated in Scheme 1.



Scheme 1. The Li₂CO₃ decomposition process involving bi-CoMnPc or bi-CoPc facilitation.

It should also be noted that, other than the oxidative decomposition path, Li₂CO₃ could also be removed through the double decomposition reaction (Equation (6)), which has

a much lower equilibrium potential (2.80 V vs. Li/Li⁺) than Equations (1)–(3) (3.71–3.82 V). There have been several 1-electron RMs reported effective for catalyzing this reaction, such as manganese phthalocyanine (MnPc) [27], ruthenium acetylacetonate (Ru(acac)₃) [28], *o*-phenylenediamine (OPD) [29], phenoxathiine (PHX) [30], etc. Therefore, this reaction should be carefully treated when investigating Li₂CO₃ decomposition mechanisms to exclude its interference.



To evaluate the effects of bi-CoMnPc on the cell performance and compare it with bi-CoPc, fixed capacity discharge–charge cycling tests were carried out for LAB coin cells with 2.5 mmol L⁻¹ of bi-CoMnPc, with 2.5 mmol L⁻¹ of bi-CoPc, or without RM in the electrolyte. The cells were tested in artificial dry air, which is composed of N₂ and O₂ (78:22, *v/v*). The discharge–charge curves are displayed in Figure 3a. With the addition of bi-CoMnPc, the mid-capacity voltage was reduced by ~260 mV from 4.02 V (without RM) to 3.76 V. This is also ~70 mV lower than that with bi-CoPc, which could be attributed to the lower redox potential of the Mn(II)/Mn(III) couple in bi-CoMnPc than that of the Co(II)/Co(III) couple in bi-CoPc, and thus reduced overpotential for Li₂O₂/LiOH decomposition. Aside from the reduction in charging potential, the RMs also exhibited an effect on elevating the discharge voltage; the discharge plateau was raised from 2.66 V without the RM to 2.71 V with bi-CoMnPc and 2.68 V with bi-CoPc. A similar phenomenon has been observed with other metal phthalocyanine complexes, such as mononuclear cobalt phthalocyanine [6] and iron phthalocyanine [31], which could be attributed to their redox mediation effect for the catalysis of oxygen reduction reactions (ORRs).

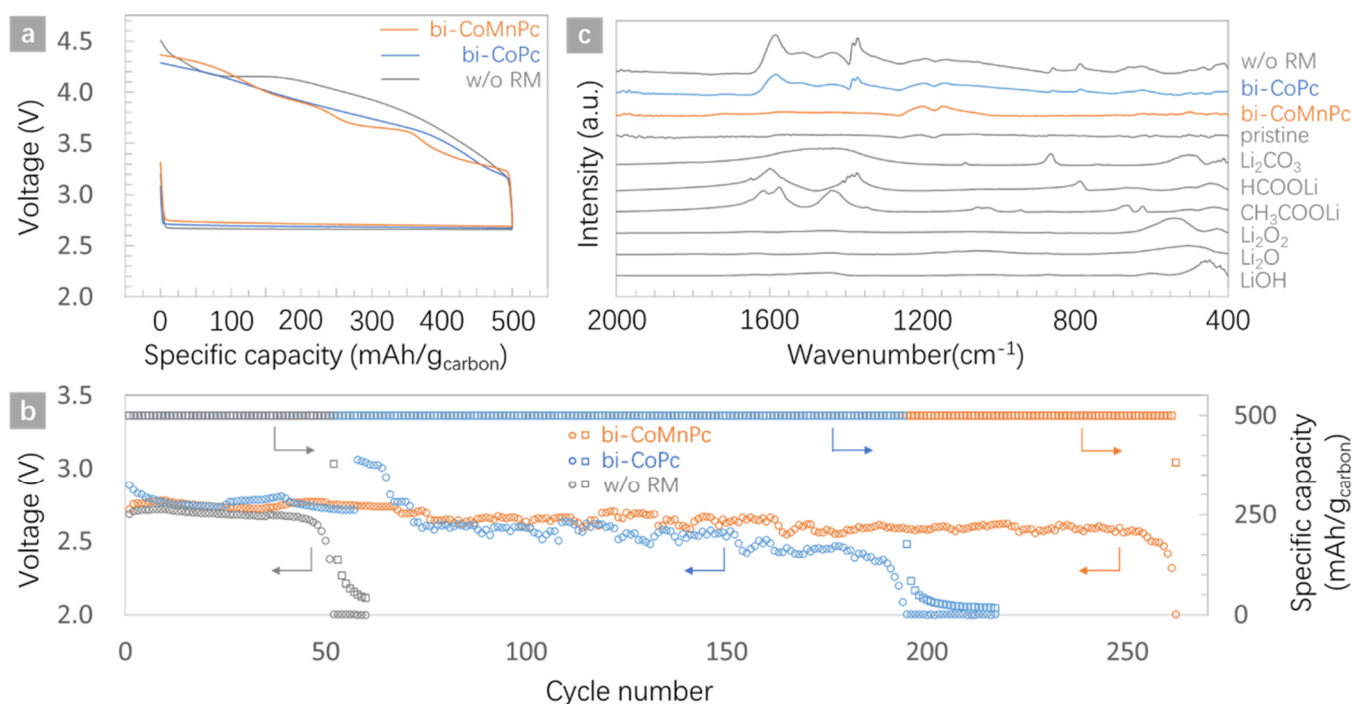


Figure 3. (a) The discharge–charge curves of LABs with bi-CoPc, bi-CoMnPc, or without RM in the first cycle, under a current density of 100 mA g⁻¹_{carbon} and a fixed capacity of 500 mAh g⁻¹_{carbon}, voltage range 2.0–4.55 V; (b) the evolution of capacity retention and terminal discharge voltage for the LABs with bi-CoPc, bi-CoMnPc, or without RM. The arrows are used to assign the terminal discharge voltage and specific capacity to different vertical axes; (c) the FTIR spectra of the air cathodes after 30 discharge–charge cycles with bi-CoPc, bi-CoMnPc, or without RM.

With RM addition in the electrolyte, the cyclic life was significantly enhanced from 52 cycles (without RM) to 193 cycles (with bi-CoPc) and 261 cycles (with bi-CoMnPc), as

shown in Figure 3b. Ex situ Fourier transform infrared (FTIR) spectroscopy in Figure 3c clearly shows that, after 30 cycles of operation, intense signals of Li_2CO_3 and lithium carboxylates became observable for the RM-free cell. In contrast, for the cell with bi-CoPc and bi-CoMnPc, the Li_2CO_3 and lithium carboxylate peaks are greatly suppressed. It is noted that the Li_2CO_3 and lithium carboxylate peaks are even less prominent for the cell with bi-CoMnPc than that with bi-CoPc, indicating bi-CoMnPc's superior suppression effect on parasitic product accumulation. To further investigate the accumulation status of parasitic products, ex situ energy dispersive spectroscopy (EDS) mapping was used to semi-quantitatively characterize the cycled air cathodes. As shown in Figures S8–S11, the oxygen content in the air cathodes with bi-CoPc or bi-CoMnPc is roughly only half of the RM-free one, indicating their good capabilities in removing parasitic products.

It has been widely perceived that high charging potential is detrimental to the cyclability of LOBs/LABs because it would induce more parasitic reactions, consuming electrolyte/carbon electrodes and accumulating solid products (such as Li_2CO_3 , lithium carboxylates, and polyesters) on the air cathode [32]. As discussed above, on the one hand, with the substitution of manganese for cobalt, the RM's functioning potential for Li_2CO_3 decomposition is raised from ~ 3.95 V (with bi-CoPc) to ~ 4.15 V (with bi-CoMnPc), but on the other hand, its functioning potential for $\text{Li}_2\text{O}_2/\text{LiOH}$ decomposition is reduced by ~ 260 mV from 3.74 V to 3.48 V. As a result of these competing effects, bi-CoMnPc apparently exhibited better performance in improving the cell cyclability, probably because Li_2O_2 is still the majority of solid-state discharge products in the CO_2 -free artificial dry air.

3. Materials and Methods

3.1. Materials

Binuclear cobalt phthalocyanine (bi-CoPc) and binuclear cobalt manganese phthalocyanine (bi-CoMnPc) were purchased from Shanghai Dibai Chemical Technologies Co., Ltd. (Shanghai, China). Tetraethylene glycol dimethyl ether (TEGDME) from Aladdin Scientific (Shanghai, China) was dried for at least 72 h over activated 3 Å molecular sieves. Li_2CO_3 was ball milled for 6 h at 400 rpm prior to use. All reagents were used as received unless specified.

3.2. Electrochemical Measurements

The cyclic voltammetry (CV), linear sweep voltammetry (LSV), and charging and discharging tests were conducted in CR2032 coin cells. The air cathode was prepared by pasting a slurry of ketjenblack (KB) EC600JD carbon black onto a piece of carbon paper (TGP-H-060, Toray, Tokyo, Japan) with a loading of ~ 0.15 $\text{mg}_{\text{carbon}} \text{cm}^{-2}$. Polytetrafluoroethylene (PTFE) was used as the binder, with KB/PTFE = 85:15 (*w/w*). The Li_2CO_3 -preloaded working electrode was prepared by casting a slurry of Li_2CO_3 -MWCNT-PVDF (4:5:1, *w/w/w*) onto a piece of carbon paper with a loading of ~ 0.5 $\text{mg}_{\text{carbon}} \text{cm}^{-2}$. A piece of lithium foil (200 μm thick) was used as the anode. The base electrolyte was 1 M lithium bis(trifluoromethanesulfonyl)imide (LiTFSI) in 140 μL of TEGDME. Electrolytes containing bi-CoPc or bi-CoMnPc were prepared by dissolving them into the base electrolyte at a concentration of 2.5 mM. A piece of glass fiber filter (Whatman GF/D, Whatman, Maidstone, UK) and a piece of PP (polypropylene) membrane (Celgard 2400, Celgard, Charlotte, NC, USA) were used as the separators. The coin cells were assembled in an Ar-filled glovebox and relaxed for 12 h, and then the tests were performed either in Ar or in a simulated dry air environment with N_2/O_2 (78:22, *v/v*). Potentiostatic and galvanostatic charging tests, as well as cycling tests, were conducted using a Neware battery testing system. The current density was set to 100 $\text{mA g}^{-1}_{\text{carbon}}$, with a cutoff voltage of 2.0 V for discharge and 4.50/4.55 V for charge. CV and LSV tests were conducted with a Solartron 1470E electrochemical workstation (Solartron Metrology, Bognor Regis, UK).

3.3. Physical Characterizations

Powder X-ray diffractograms (XRD) were obtained on a D8 ADVANCE DaVinci diffractometer (Bruker, Billerica, MA, USA) with Cu K α radiation ($\lambda = 1.5418 \text{ \AA}$). Fourier transform infrared (FTIR) spectra were collected on a Nicolet 6700 spectrometer (Thermo Fisher Scientific, Waltham, MA, USA) in transmission mode or on a Cary 660+620 spectrometer (Agilent, Santa Clara, CA, USA) in attenuated total reflectance (ATR) mode. Scanning electron microscopy (SEM) was performed on a Hitachi S4800 (Hitachi, Tokyo, Japan) unit or on a Quanta 250 FEG unit (FEI, Hillsboro, OR, USA).

3.4. Computation Methods

The DFT calculation was performed by using the Gaussian 16 [33], xTB (version 6.3.2) [34,35], and ORCA 5.0 [36] programs. Structural optimization and frequency analysis were performed at the GFN2-xTB level as interfaced into the Gaussian 16 program using the gau_xtb code [37] to obtain the thermal correction to Gibbs energy in the gas phase. Stationary points were optimized without symmetry constraints, and their nature was confirmed by vibrational frequency analysis. All structures given are at minimal points and have no imaginary frequencies. Then, more accurate single-point energies were obtained at the ω B97X [38]-D3BJ [39,40]/def2-TZVPP [41] level with ORCA. The Gibbs free energy G was calculated as $G = E$ (single-point energies obtained by wb97X-D3BJ/def2-TZVPP) + E (thermal correction to Gibbs by GFN2-xTB). And ΔG was calculated by $\Delta G = \Delta E + \Delta ZPE - T\Delta S$, where ΔE , ΔZPE , T , and ΔS indicated the single-point energy change, zero-point energy change, temperature, and entropy change, respectively. In the decomposition pathways, the intermediate label * represents adsorption on the phthalocyanine structure; otherwise, it means in the gas phase state. The total charge of the structures is considered with the change in the adsorption state, which is the sum of the charges of the binuclear metal phthalocyanine and the adsorption structure. The natural bond orbital (NBO) [42–47] calculations were performed to obtain further information.

4. Conclusions

The effects of central metal ions in binuclear metal phthalocyanines have been investigated in terms of their catalytic activity towards Li_2CO_3 decomposition. DFT calculations indicate that the key intermediate peroxydicarbonate ($^*\text{C}_2\text{O}_6^{2-}$) is stabilized by bi-CoPc $^{2+}$ and bi-CoMnPc $^{2+}$, which is accountable for their improved catalytic activity compared to bi-CoPc $^+$ /bi-CoMnPc $^+$ and pristine bi-CoPc/bi-CoMnPc. With one central metal ion substituted by manganese for cobalt, the bi-CoMnPc's second active redox couple for catalyzing Li_2CO_3 decomposition shifts from the second Co(II)/Co(III) couple in the central metal ion to the Pc(-2)/Pc(-1) couple in the phthalocyanine ring. In artificial dry air, the LAB cell with bi-CoMnPc in electrolyte exhibited 261 cycles under a fixed capacity of $500 \text{ mAh g}^{-1}_{\text{carbon}}$ and current density of $100 \text{ mA g}^{-1}_{\text{carbon}}$, significantly better than the RM-free cell (62 cycles) and even the cell with bi-CoPc (193 cycles). We hope this work sheds new insights into the mechanisms of RM-facilitated Li_2CO_3 decomposition and designs more efficient Li_2CO_3 decomposing RMs.

Supplementary Materials: The following supporting information can be downloaded at <https://www.mdpi.com/article/10.3390/molecules29092034/s1>, Figure S1: The structures of bi-CoPc and bi-CoMnPc. Figure S2: The Li_2CO_3 decomposition pathways on bi-CoPc $^{2+}$ and corresponding structures with bi-CoPc $^{2+} \rightarrow$ bi-CoPc. Figure S3: The Li_2CO_3 decomposition pathways on pristine bi-CoPc $^{2+}$ and the corresponding structures with 2bi-CoPc $^{2+} \rightarrow$ 2bi-CoPc $^+$. Figure S4: The Li_2CO_3 decomposition pathways on bi-CoPc $^+$ and the corresponding structures with 2bi-CoPc $^+ \rightarrow$ 2bi-CoPc. Figure S5: The Li_2CO_3 decomposition pathways on pristine bi-CoMnPc $^{3+}$ and the corresponding structures with bi-CoMnPc $^{3+} \rightarrow$ bi-CoMnPc $^+$. Figure S6: The Li_2CO_3 decomposition pathways on pristine bi-CoMnPc $^{3+}$ and the corresponding structures with 2bi-CoMnPc $^{3+} \rightarrow$ 2bi-CoMnPc $^{2+}$. Figure S7: The Li_2CO_3 decomposition pathways on pristine bi-CoMnPc $^{2+}$ and the corresponding structures with 2bi-CoMnPc $^{2+} \rightarrow$ 2bi-CoMnPc $^+$. Figure S8: The SEM images and EDS mapping results of carbon and oxygen for the air cathode (a) without RM, (b) with bi-CoPc and (c) with bi-CoMnPc after 1 discharge-

charge cycle. Figure S9: The SEM images and EDS mapping results of carbon and oxygen for the air cathode (a) without RM, (b) with bi-CoPc and (c) with bi-CoMnPc after 10 discharge-charge cycles. Figure S10: The SEM images and EDS mapping results of carbon and oxygen for the air cathode (a) without RM, (b) with bi-CoPc and (c) with bi-CoMnPc after 30 discharge-charge cycles. Figure S11: The oxygen content in the cycled air cathodes according to EDS results.

Author Contributions: Conceptualization, Z.L.; methodology, Z.L. and S.Z.; investigation, Q.Y. and L.Y.; data curation, Q.Y. and L.Y.; validation, Q.Y., L.Y. and H.H. (Haoshen Huang); formal analysis, Z.L. and S.Z.; writing—original draft preparation, Q.Y., L.Y., Z.L. and S.Z.; writing—review and editing, Z.C. and H.H. (Haiyong He); funding acquisition, Z.L., S.Z. and Z.C. All authors have read and agreed to the published version of the manuscript.

Funding: This research was funded by the Key Research and Development Program of Zhejiang Province (grant number 2023C01102), the Ningbo S&T Innovation 2025 Major Special Program (grant number 2022Z022), and the Ningbo Science and Technology Project (grant number 2022-DST-004).

Institutional Review Board Statement: Not applicable.

Informed Consent Statement: Not applicable.

Data Availability Statement: The data presented in this study are available in article and Supplementary Materials.

Acknowledgments: The authors would like to thank Jiahao Song and Junwen Zheng for their assistance in manuscript review and editing.

Conflicts of Interest: The authors declare no conflicts of interest.

References

1. Kwak, W.-J.; Rosy, Sharon, D.; Xia, C.; Kim, H.; Johnson, L.R.; Bruce, P.G.; Nazar, L.F.; Sun, Y.-K.; Frimer, A.A.; et al. Lithium-Oxygen Batteries and Related Systems: Potential, Status, and Future. *Chem. Rev.* **2020**, *120*, 6626–6683. [[CrossRef](#)] [[PubMed](#)]
2. Liu, T.; Vivek, J.P.; Zhao, E.W.; Lei, J.; Garcia-Araez, N.; Grey, C.P. Current Challenges and Routes Forward for Nonaqueous Lithium–Air Batteries. *Chem. Rev.* **2020**, *120*, 6558–6625. [[CrossRef](#)] [[PubMed](#)]
3. Chen, K.; Yang, D.-Y.; Huang, G.; Zhang, X.-B. Lithium–Air Batteries: Air-Electrochemistry and Anode Stabilization. *Acc. Chem. Res.* **2021**, *54*, 632–641. [[CrossRef](#)] [[PubMed](#)]
4. Kang, J.-H.; Lee, J.; Jung, J.-W.; Park, J.; Jang, T.; Kim, H.-S.; Nam, J.-S.; Lim, H.; Yoon, K.R.; Kim, I.-D.; et al. Lithium–Air Batteries: Air-Breathing Challenges and Perspective. *ACS Nano* **2020**, *14*, 14549–14578. [[CrossRef](#)] [[PubMed](#)]
5. Zhao, Z.; Huang, J.; Peng, Z. Achilles’ Heel of Lithium–Air Batteries: Lithium Carbonate. *Angew. Chem. Int. Ed.* **2017**, *57*, 3874–3886. [[CrossRef](#)] [[PubMed](#)]
6. Liu, Z.; Zhang, Y.; Jia, C.; Wan, H.; Peng, Z.; Bi, Y.; Liu, Y.; Peng, Z.; Wang, Q.; Li, H.; et al. Decomposing lithium carbonate with a mobile catalyst. *Nano Energy* **2017**, *36*, 390–397. [[CrossRef](#)]
7. Wang, X.-G.; Wang, C.; Xie, Z.; Zhang, X.; Chen, Y.; Wu, D.; Zhou, Z. Improving Electrochemical Performances of Rechargeable Li–CO₂ Batteries with an Electrolyte Redox Mediator. *ChemElectroChem* **2017**, *4*, 2145–2149. [[CrossRef](#)]
8. Mota, F.M.; Kang, J.-H.; Jung, Y.; Park, J.; Na, M.; Kim, D.H. Mechanistic Study Revealing the Role of the Br₃[−]/Br₂ Redox Couple in CO₂-Assisted Li–O₂ Batteries. *Adv. Energy Mater.* **2020**, *10*, 1903486. [[CrossRef](#)]
9. Chen, J.; Zou, K.; Ding, P.; Deng, J.; Zha, C.; Hu, Y.; Zhao, X.; Wu, J.; Fan, J.; Li, Y. Conjugated Cobalt Polyphthalocyanine as the Elastic and Reprocessable Catalyst for Flexible Li–CO₂ Batteries. *Adv. Mater.* **2019**, *31*, 1805484. [[CrossRef](#)]
10. Huang, S.; Li, Z.; Liu, Z.; Yan, Q.; Ma, B.; Wang, D.; Wei, F.; Chen, Z.; He, H. Surface Enrichment of Redox Mediator for Long-Cyclable Lithium–Air Batteries. *Energy Fuels* **2023**, *37*, 11465–11471. [[CrossRef](#)]
11. Zhu, C.; Wang, Y.; Shuai, L.; Tang, Y.; Qiu, M.; Xie, J.; Liu, J.; Wen, W.; Chen, H.; Nan, S.; et al. Remarkable improvement of cyclic stability in Li–O₂ batteries using ruthenocene as a redox mediator. *Chin. Chem. Lett.* **2020**, *31*, 1997–2002. [[CrossRef](#)]
12. Wan, H.; Sun, Y.; Yu, J.; Shi, Q.; Zhu, Y.; Qian, Y. A chiral salen-Co(II) complex as soluble redox mediator for promoting the electrochemical performance of Li–O₂ batteries. *Nano Res.* **2022**, *15*, 8101–8108. [[CrossRef](#)]
13. Ko, S.; Yoo, Y.; Choi, J.; Lim, H.-D.; Park, C.B.; Lee, M. Discovery of organic catalysts boosting lithium carbonate decomposition toward ambient air operational lithium–air batteries. *J. Mater. Chem. A* **2022**, *10*, 20464. [[CrossRef](#)]
14. Pipes, R.; Bhargava, A.; Manthiram, A. Phenyl Disulfide Additive for Solution-Mediated Carbon Dioxide Utilization in Li–CO₂ Batteries. *Adv. Energy Mater.* **2019**, *9*, 1900453. [[CrossRef](#)]
15. Xiong, Q.; Huang, G.; Zhang, X.-B. High-Capacity and Stable Li–O₂ Batteries Enabled by a Trifunctional Soluble Redox Mediator. *Angew. Chem. Int. Ed.* **2020**, *59*, 19311–19319. [[CrossRef](#)]
16. Jiang, F.; Ma, L.; Sun, J.; Guo, L.; Peng, Z.; Cui, Z.; Li, Y.; Guo, X.; Zhang, T. Deciphering the Enigma of Li₂CO₃ Oxidation Using a Solid-State Li–Air Battery Configuration. *ACS Appl. Mater. Interfaces* **2021**, *13*, 14321–14326. [[CrossRef](#)]

17. Yang, S.; He, P.; Zhou, H. Exploring the electrochemical reaction mechanism of carbonate oxidation in Li–air/CO₂ battery through tracing missing oxygen. *Energy Environ. Sci.* **2016**, *9*, 1650–1654. [CrossRef]
18. Mahne, N.; Renfrew, S.E.; McCloskey, B.D.; Freunberger, S.A. Electrochemical Oxidation of Lithium Carbonate Generates Singlet Oxygen. *Angew. Chem. Int. Ed.* **2018**, *57*, 5529–5533. [CrossRef]
19. Cao, D.; Tan, C.; Chen, Y. Oxidative decomposition mechanisms of lithium carbonate on carbon substrates in lithium battery chemistries. *Nat. Commun.* **2022**, *13*, 4908. [CrossRef]
20. Lever, A.B.P.; Minor, P.C.; Wilshire, J.P. Electrochemistry of Manganese Phthalocyanine in Nonaqueous Media. *Inorg. Chem.* **1981**, *20*, 2550–2553. [CrossRef]
21. Lin, C.-L.; Lee, C.-C.; Ho, K.-C. Spectroelectrochemical studies of manganese phthalocyanine thin films for applications in electrochromic devices. *J. Electroanal. Chem.* **2002**, *524–525*, 81–89. [CrossRef]
22. Kobayashi, N.; Lam, H.; Nevin, W.A.; Janda, P.; Leznoff, C.C.; Koyama, T.; Monden, A.; Shirai, H. Synthesis, spectroscopy, electrochemistry, spectroelectrochemistry, Langmuir-Blodgett film formation, and molecular orbital calculations of planar binuclear phthalocyanines. *J. Am. Chem. Soc.* **1994**, *116*, 879–890. [CrossRef]
23. Lim, H.-D.; Lee, B.; Zheng, Y.; Hong, J.; Kim, J.; Gwon, H.; Ko, Y.; Lee, M.; Cho, K.; Kang, K. Rational design of redox mediators for advanced Li–O₂ batteries. *Nat. Energy* **2016**, *1*, 16066. [CrossRef]
24. Chen, Y.; Gao, X.; Johnson, L.R.; Bruce, P.G. Kinetics of lithium peroxide oxidation by redox mediators and consequences for the lithium–oxygen cell. *Nat. Commun.* **2018**, *9*, 767. [CrossRef] [PubMed]
25. Ahn, S.; Zor, C.; Yang, S.; Lagnoni, M.; Dewar, D.; Nimmo, T.; Chau, C.; Jenkins, M.; Kibler, A.J.; Pateman, A.; et al. Why charging Li–air batteries with current low-voltage mediators is slow and singlet oxygen does not explain degradation. *Nat. Chem.* **2023**, *15*, 1022–1029. [CrossRef] [PubMed]
26. Qiao, Y.; Yi, J.; Guo, S.; Sun, Y.; Wu, S.; Liu, X.; Yang, S.; He, P.; Zhou, H. Li₂CO₃-free Li–O₂/CO₂ battery with peroxide discharge product. *Energy Environ. Sci.* **2018**, *11*, 1211–1217. [CrossRef]
27. Kim, B.; Shin, K.; Henkelman, G.; Ryu, W.-H. CO₂-mediated porphyrin catalysis in reversible Li–CO₂ cells. *Chem. Eng. J.* **2023**, *477*, 147141. [CrossRef]
28. Lian, Z.; Lu, Y.; Ma, S.; Wang, L.; Li, Z.; Liu, Q. An integrated strategy for upgrading Li–CO₂ batteries: Redox mediator and separator modification. *Chem. Eng. J.* **2022**, *450*, 138400. [CrossRef]
29. Wang, L.; Lu, Y.; Ma, S.; Lian, Z.; Gu, X.; Li, J.; Li, Z.; Liu, Q. Optimizing CO₂ reduction and evolution reaction mediated by o-phenylenediamine toward high performance Li–CO₂ battery. *Electrochim. Acta* **2022**, *419*, 140424. [CrossRef]
30. Cao, D.; Liu, X.; Yuan, X.; Yu, F.; Chen, Y. Redox Mediator-Enhanced Performance and Generation of Singlet Oxygen in Li–CO₂ Batteries. *ACS Appl. Mater. Interfaces* **2021**, *13*, 39341–39346. [CrossRef]
31. Sun, D.; Shen, Y.; Zhang, W.; Yu, L.; Yi, Z.; Yin, W.; Wang, D.; Huang, Y.; Wang, J.; Wang, D.; et al. A Solution-Phase Bifunctional Catalyst for Lithium–Oxygen Batteries. *J. Am. Chem. Soc.* **2014**, *136*, 8941–8946. [CrossRef] [PubMed]
32. Ottakam Thotiyil, M.M.; Freunberger, S.A.; Peng, Z.; Bruce, P.G. The Carbon Electrode in Nonaqueous Li–O₂ Cells. *J. Am. Chem. Soc.* **2013**, *135*, 494–500. [CrossRef]
33. Frisch, M.J.; Trucks, G.W.; Schlegel, H.B.; Scuseria, G.E.; Robb, M.A.; Cheeseman, J.R.; Scalmani, G.; Barone, V.; Petersson, G.A.; Nakatsuji, H.; et al. *Gaussian 16*; Gaussian, Inc.: Wallingford, CT, USA, 2016.
34. Grimme, S.; Bannwarth, C.; Shushkov, P. A Robust and Accurate Tight-Binding Quantum Chemical Method for Structures, Vibrational Frequencies, and Noncovalent Interactions of Large Molecular Systems Parametrized for All spd-Block Elements (Z = 1–86). *J. Chem. Theory Comput.* **2017**, *13*, 1989–2009. [CrossRef] [PubMed]
35. Bannwarth, C.; Ehlert, S.; Grimme, S. GFN2-xTB—An Accurate and Broadly Parametrized Self-Consistent Tight-Binding Quantum Chemical Method with Multipole Electrostatics and Density-Dependent Dispersion Contributions. *J. Chem. Theory Comput.* **2019**, *15*, 1652–1671. [CrossRef] [PubMed]
36. Neese, F. The ORCA program system. *WIREs Comput. Mol. Sci.* **2011**, *2*, 73–78. [CrossRef]
37. Lu, T. Gau_Xtb: A Gaussian Interface for Xtb Code. Available online: https://sobereva.com/soft/gau_xtb (accessed on 15 August 2023).
38. Chai, J.-D.; Head-Gordon, M. Systematic optimization of long-range corrected hybrid density functionals. *J. Chem. Phys.* **2008**, *128*, 084106. [CrossRef] [PubMed]
39. Grimme, S.; Ehrlich, S.; Goerigk, L. Effect of the damping function in dispersion corrected density functional theory. *J. Comput. Chem.* **2011**, *32*, 1456–1465. [CrossRef] [PubMed]
40. Grimme, S.; Antony, J.; Ehrlich, S.; Krieg, H. A consistent and accurate ab initio parametrization of density functional dispersion correction (DFT-D) for the 94 elements H–Pu. *J. Chem. Phys.* **2010**, *132*, 154104. [CrossRef]
41. Weigend, F.; Ahlrichs, R. Balanced basis sets of split valence, triple zeta valence and quadruple zeta valence quality for H to Rn: Design and assessment of accuracy. *Phys. Chem. Chem. Phys.* **2005**, *7*, 3297–3305. [CrossRef]
42. Reed, A.E.; Curtiss, L.A.; Weinhold, F. Intermolecular Interactions from a Natural Bond Orbital, Donor-Acceptor Viewpoint. *Chem. Rev.* **1988**, *88*, 899–926. [CrossRef]
43. Carpenter, J.E.; Weinhold, F.J. Analysis of the geometry of the hydroxymethyl radical by the “different hybrids for different spins” natural bond orbital procedure. *J. Mol. Struct. Theochem.* **1988**, *46*, 41–62. [CrossRef]
44. Reed, A.E.; Weinstock, R.B.; Weinhold, F.J. Natural Atomic Orbitals and Natural Population Analysis. *J. Chem. Phys.* **1985**, *83*, 735–746. [CrossRef]

45. Reed, A.E.; Weinhold, F.J. Natural Localized Molecular Orbitals. *J. Chem. Phys.* **1985**, *83*, 1736–1740. [[CrossRef](#)]
46. Reed, A.E.; Weinhold, F.J. Natural Bond Orbital Analysis of Near-Hartree-Fock Water Dimer. *J. Chem. Phys.* **1983**, *78*, 4066–4073. [[CrossRef](#)]
47. Foster, J.P.; Weinhold, F.J. Natural Hybrid Orbitals. *J. Am. Chem. Soc.* **1980**, *102*, 7211–7218. [[CrossRef](#)]

Disclaimer/Publisher’s Note: The statements, opinions and data contained in all publications are solely those of the individual author(s) and contributor(s) and not of MDPI and/or the editor(s). MDPI and/or the editor(s) disclaim responsibility for any injury to people or property resulting from any ideas, methods, instructions or products referred to in the content.